The Planetary Science Journal, 4:187 (11pp), 2023 October https://doi.org/10.3847/PSJ/acf5e9

Roughness and Angularity of Fragments from Meteorite Disruption Experiments

Gabriel Gowman[1], Desireé Cotto-Figueroa[2], Andrew Ryan[1], Laurence A. J. Garvie[3,4], Christian G. Hoover[5], and Erik Asphaug[1]
[1] Lunar and Planetary Laboratory, University of Arizona, Tucson, AZ 85721, USA; gowmang@arizona.edu
[2] Department of Physics and Electronics, University of Puerto Rico at Humacao, Humacao, PR 00792, USA
[3] Buseck Center for Meteorite Studies, Arizona State University, Tempe, AZ 85287, USA
[4] School of Earth and Space Exploration, Arizona State University, Tempe, AZ 85287, USA
[5] School of Sustainable Engineering and the Built Environment, Arizona State University, Tempe, AZ 85281, USA
Received 2023 May 10; revised 2023 August 25; accepted 2023 August 29; published 2023 October 4

Abstract

In this study, we set out to explore the relationship between fracture roughness and sample strength. We analyze 45 fragments of Aba Panu, Allende, and Tamdakht, three meteorites that have been strength-tested to disruption, to determine whether their shape or texture is correlated with measured compressive strength. A primary goal is to understand whether these exterior properties correlate with more challenging strength-related measurements. We first scan the samples and construct high-fidelity 3D models. The gradient-based angularity index AI_g and the rms slope roughness metric θ_{rms} are applied to all nine samples, and their validity and any correlation between them are analyzed. We find that different sample subsets show significant variation in both correlation strength and direction. We also find AI_g to be of questionable validity in its application to highly angular samples. Based on our methodology and results, we do not find sufficient separation between the roughness values of samples to allow distinct identification of the three meteorites based on roughness alone. Additionally, neither metric shows a strong correlation with the strength of individual fragments. We do find, however, that the spread of the fragment strength distribution within a given meteorite has some correlation with its average roughness metric. Increased fragment roughness may imply greater structural heterogeneity and therefore potentially weaker behavior at larger sizes. We only have significant data sets for two meteorites, however, which are insufficient to correlate meteorite fracture roughness to meteorite strength in any simple way.

Unified Astronomy Thesaurus concepts: Meteorites (1038); Carbonaceous chondrites (200); Chondrites (228); Computational methods (1965); Small Solar System bodies (1469)

1. Introduction

Meteorites are fragments of asteroids and nearby planets. As such, they contain unique information about solar system physics and chemistry, as well as planetary origins and geology. Particle roughness is known to play a significant role in controlling interparticle contact forces on a microscopic level, as well as macroscopic effects such as stiffness and shear strength for granular materials (Su et al. 2019). Recent work has sought to extend this connection between contact forces and particle shape to meteorite fragments, examining cohesive forces in crushed meteorite powder (Nagaashi et al. 2021; Nagaashi & Nakamura 2023), and to asteroid-scale bodies for which cohesion may be critical in maintaining structural integrity while rotating (Persson & Biele 2022). For other materials such as concretes, finer-grained samples have been found to possess higher compressive strength and smoother fracture surfaces (Ficker et al. 2010). We seek analogous relationships for centimeter-scale meteorite samples, connecting textural properties to strength. If such a relationship could be found, it could potentially preserve the finite supply of meteorite and especially asteroid samples from needing to be crushed in order to measure strength. Instead, noninvasive methods such as the scanning procedure presented in this work could be used to constrain strength properties without damaging the samples.

Here we report on the roughness and angularity of fragments produced in destructive stress-to-failure experiments. The immediate goal is to seek correlations between rock fracture roughness, which would be optically measurable at an asteroid at larger scales, and strength properties. This report focuses primarily on the quantification of angularity and roughness for the broken fragments. We prepare for future work connecting these data and methods to measured strength properties. We study 45 samples from three different meteorites (Section 2) that were involved in a series of compression experiments (Cotto-Figueroa et al. 2016; Rabbi et al. 2021). Section 3 describes our 3D scanning method and the roughness and angularity analysis. Section 4 presents our measurements and findings, discussed in Section 5. Section 6 provides broad takeaways and suggestions for future work.

2. Samples

This work presents results for a total of 45 meteorite samples. Five come from the L3 meteorite Aba Panu (Gattacceca et al. 2020), 11 from the CV3 meteorite Allende (King et al. 1969), and the remaining 29 from the H5 meteorite Tamdakht (Weisberg et al. 2009). Most are fragments from centimeter-sized cubes that were subjected to destructive strength testing (Cotto-Figueroa et al. 2016; Rabbi et al. 2021) to measure the compressive strength and failure stress of these meteorites and are labeled “shards.” These samples serve as the main focus of our analysis. Other

Table 1
Selection of Prior Data Related to the Studied Meteorites

Meteorite	Class	ρ_b (g cm^{-3})	ρ_g (g cm^{-3})	P (%)	$\bar{\sigma}$ (MPa)	Weibull m
Aba Panu	L3	3.41 ± 0.03	3.53 ± 0.02	3.1 ± 0.6	438.4	...
Allende	CV3	2.88 ± 0.05	3.53 ± 0.14	19.0 ± 3.3	35.4	4.46 ± 0.06
Tamdakht	H5	3.60 ± 0.015	3.75 ± 0.04	4.08 ± 0.72	124.2	1.73 ± 0.06

Note. Bulk and grain densities ρ_b and ρ_g, porosity P (Britt & Consolmagno 2003; Li et al. 2019; Flynn et al. 2023), average compressive strength $\bar{\sigma}$ (Cotto-Figueroa et al. 2016; Rabbi et al. 2021), and Weibull parameter m (Cotto-Figueroa et al. 2016).

Table 2
Samples Used in This Analysis, and the Masses M, Volumes V, and Bulk Densities ρ_b Obtained

Sample ID	M (g)	V (cm^3)	ρ_b (g cm^{-3})	No. Facets	σ (MPa)	AI$_g$	$\theta_{\rm rms}$ (deg)
AP-S-10-1	0.283(1)	0.083	3.412	96,394	578.0	9.854	18.099
AP-S-10-2	0.206(3)	0.060	3.460	83,729	578.0	9.700	19.081
AP-S-10-3	0.184(7)	0.054	3.407	73,441	578.0	8.205	17.101
AP-S-10-4	0.371(4)	0.109	3.419	131,743	578.0	7.048	19.000
AP-S-10-10	0.035(0)	0.010	3.456	22,445	578.0	7.416	21.878
A-RB-1	4.826(4)	1.653	2.919	1,012,898	...	4.964	16.357
A-RB-7	1.847(3)	0.635	2.910	459,665	...	4.369	16.584
A-RB-8	3.701(0)	1.281	2.888	763,296	...	4.065	15.071
A-RB-10	2.873(3)	0.983	2.922	574,528	...	3.272	14.759
A-RB-12	5.795(8)	1.991	2.912	1,185,043	...	4.266	14.590
A-RB-20	1.022(5)	0.359	2.847	313,988	...	2.674	16.526
A-RB-24	2.024(9)	0.702	2.883	581,492	...	4.975	16.871
A-RF-1	4.662	1.602	2.910	743,770	...	5.383	18.032
A-RF-2	6.148	2.099	2.930	842,052	...	3.577	17.875
A-S-AllB-1	2.862	0.992	2.886	757,052	41.1	11.260	16.500
A-S-AllB-2	2.488	0.854	2.914	523,715	41.1	9.105	16.409
T-RF-1	8.549	2.482	3.445	1,012,107	...	4.474	18.746
T-RF-2	3.643	1.031	3.534	709,859	...	24.102	17.111
T-RF-3	5.310	1.504	3.530	873,449	...	9.564	17.916
T-S-t1a-1	0.345(2)	0.108	3.195	139,089	83.6	12.532	17.256
T-S-t1a-2	0.286(5)	0.084	3.431	104,473	83.6	13.169	17.237
T-S-t1a-3	0.190(2)	0.056	3.379	108,412	83.6	9.150	19.208
T-S-t1a-4	0.287(7)	0.089	3.245	205,959	83.6	20.939	21.175
T-S-t1a-5	0.171(0)	0.052	3.278	109,432	83.6	20.281	21.175
T-S-t1b-1	1.012(3)	0.305	3.323	330,904	120.5	11.559	19.314
T-S-t1b-2	1.059(3)	0.315	3.365	225,814	120.5	13.762	16.868
T-S-t1b-3	0.309(7)	0.096	3.230	136,379	120.5	11.769	19.772
T-S-t1b-4	1.178(1)	0.356	3.308	355,369	120.5	8.988	19.175
T-S-t1c-1	0.558(5)	0.162	3.458	159,870	130.7	10.421	18.894
T-S-t1c-2	0.543(3)	0.150	3.622	147,744	130.7	11.998	19.488
T-S-t1c-3	0.413(1)	0.124	3.340	181,116	130.7	8.420	19.014
T-S-t1c-4	3.367(5)	1.030	3.270	433,461	130.7	11.294	19.982
T-S-t1d-1	2.141(2)	0.678	3.159	515,279	84.3	12.119	17.646
T-S-t1d-2	0.989(1)	0.290	3.407	281,312	84.3	9.451	16.587
T-S-t1d-3	1.680(2)	0.501	3.356	248,710	84.3	10.796	19.347
T-S-t1d-4	0.304(5)	0.077	3.958	142,013	84.3	10.393	19.537
T-S-t1e-2	0.213(8)	0.052	4.127	86,462	186.0	5.394	18.645
T-S-t1e-3	3.491(7)	1.065	3.280	405,290	186.0	11.312	19.514
T-S-t1g-1	0.749(4)	0.224	3.340	264,097	247.4	13.462	18.309
T-S-t1g-2	0.220(9)	0.063	3.483	130,508	247.4	8.358	19.679
T-S-t1g-3	0.726(3)	0.218	3.337	209,781	247.4	10.606	17.952
T-S-t1g-4	1.983(2)	0.579	3.426	420,106	247.4	9.881	18.358
T-S-t1h-2	0.156(3)	0.045	3.440	95,992	120.5	16.590	20.221
T-S-t3a-1	1.680	0.484	3.474	353,229	97.0	11.219	17.042
T-S-t3a-2	3.349	0.970	3.453	611,360	97.0	10.027	18.105

Note. The "No. Facets" column lists the number of facets in the constructed 3D models shown in Figure 2, and the σ column lists measured strength values of the samples' source cubes, where applicable. The final columns list global values for the angularity index AI$_g$ and the rms slope $\theta_{\rm rms}$, plotted in Figure 7.

pieces broke off their source meteorites at other stages of processing the meteorite samples and are included to expand the sample, given that fragmentation and abrasion both contribute naturally to asteroid material roughness and offer preliminary data regarding how abrasion or other processes may affect the samples. Table 1 lists a selection of prior

Figure 1. Photograph of nine meteorite samples used in this analysis, along with a 1 cm square for scale reference. Top row: scale square, Allende—A-RF-1, A-RF-2, A-S-AllB-1, A-S-AllB-2. Bottom row: Tamdakht—T-RF-1, T-RF-2, T-RF-3, T-S-t3a-1, T-S-t3a-2.

knowledge regarding the three source meteorites. The Weibull parameter m describes the homogeneity of strength values for the collection of samples studied from a given meteorite (or other sample set). Lower m indicates greater variation in strength properties between similar samples and, in general, more flaws, cracks, and porosity that are sites for crack initiation (Cotto-Figueroa et al. 2016). It should be noted that the Tamdakht samples showed dramatically more variation in compressive strength than the Allende samples in testing by Cotto-Figueroa et al. (2016).

The samples were scanned to construct 3D models; from these, we derived their volumes and obtained bulk densities based on their measured masses. The Allende sample densities were consistent with the previous measurement of 2.88 ± 0.05 g cm^{-3} (Britt & Consolmagno 2003), while Tamdakht sample densities were in general slightly lower than the previously measured 3.60 g cm^{-3} (Li et al. 2019). Aba Panu samples were also near the expected value of 3.41 g cm^{-3} (Flynn et al. 2023); however, several samples from both Aba Panu and Tamdakht were outside of prior measurements' uncertainty ranges. The list of samples, along with their identifiers, masses (M), volumes (V), and bulk densities (ρ_b), is included in Table 2, as well as the number of facets in the corresponding 3D models (see Section 3). Identifiers are based on the meteorite name and the shape descriptor, where the latter is "shard" (S) if the sample is a remnant of a machined cube shattered during strength testing, or "random fragment" (RF) or "random bag" (RB) if it broke off from a source meteorite or prior sample at a different time. RB fragments were originally stored loosely in a bag and allowed to contact each other, which may affect the surface roughness. We include RB fragments as an extension of our Allende meteorite sample set, seeing as abrasion by seismic motion, particle overturn, space weathering, and other processes (Tsuchiyama et al. 2011) might all occur on an asteroid. Samples A-S-AllB-1 and A-S-AllB-2 come from sample A10 of Cotto-Figueroa et al. (2016). Tamdakht shards were obtained from eight different cubes. In most cases, four broken pieces from each cube were selected for analysis, with the few cubes with lesser representation having few sufficiently large fragments. The "σ" column in Table 2 lists measured compressive strength values (Cotto-Figueroa et al. 2016). Nine selected samples from Allende and Tamdakht are shown in Figure 1.

3. Methods

3.1. Scanning

The samples were scanned using a Polyga Compact C506 3D structured-light scanner. This instrument operates by projecting blue light patterns as a planar sheet onto the object. The patterns consist of parallel stripes of varying thickness. A pair of panchromatic cameras obtain off-axis images, where the profile of the illuminated stripes depends on local topography (Bell et al. 2016). The FlexScan3D software package that comes with the C506 scanner was used to operate the instrument and to convert collected data into 3D point clouds and ultimately triangular surface meshes. The scanner has a spatial resolution (point-to-point distance) of 20–25 μm and accuracy $\geqslant 12$ μm. Samples were scanned using approximately 24–30 individual orientations to accurately measure the full 3D object. FlexScan3D software was used to capture and combine the various scans to construct complete models. The combination step required close alignment of scans such that software can recognize similar features of successive scans. This presented a challenge for highly smooth and featureless samples, as well as for very flat samples, for which the difficulty arose when connecting the top and bottom of the incomplete model. The final 3D models were coarsened slightly (see Section 3.2.1) to provide consistent baselines for the application of our metrics. Two selected 3D models are shown in Figure 2.

3.2. Angularity and Roughness Metrics

3.2.1. Roughness

The samples' roughness was quantified using the rms slope method previously applied to asteroid (101955) Bennu by Rozitis et al. (2020). Equation (1) defines this calculation, where a_i is the area of a particular facet and θ_i is the angle of that facet, measured relative to a local horizontal. These are summed over all N facets in the mesh. The angles are weighted by their projected areas $a_i|\cos\theta_i|$, reducing the effect of tiny or sharply angled facets:

$$\theta_{\rm rms} = \sqrt{\frac{\sum_{i=1}^{N} \theta_i^2 a_i |\cos\theta_i|}{\sum_{i=1}^{N} a_i |\cos\theta_i|}}. \tag{1}$$

The local normal was determined by decimating the scans using MeshLab software (Cignoni et al. 2008). This software offers "clustering simplification," in which the model is

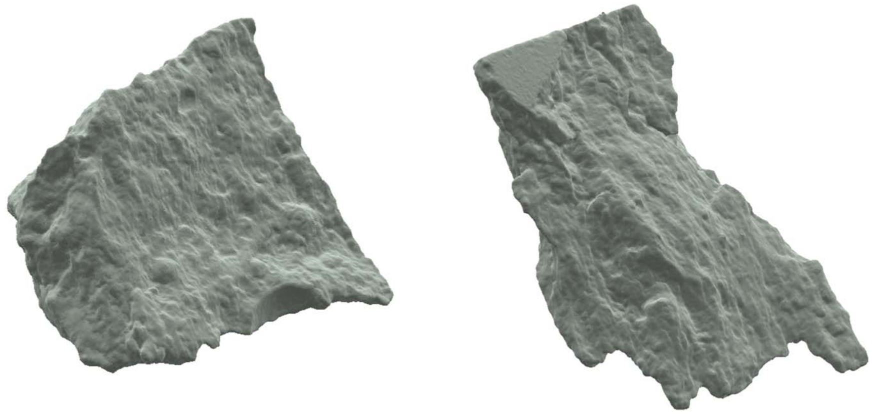

(a) Sample A-RF-1 (b) Sample T-S-t3a-2

Figure 2. 3D models of selected samples from Allende (A-RF-1) and Tamdakht (T-S-t3a-2).

covered in a grid of cubic cells of a specified size. The model is then decimated according to those cells, unifying features within each region and simplifying to a desirable level of detail. This algorithm removes fine detail from the model, reducing the overall number of faces and vertices, while preserving the overall shape and coarse texture. That lost detail is the desired "roughness" to be quantified here. The local horizontal was defined via the planes of the decimated scans' facets, and a nearest neighbor approach was used to assess which of the original model's facets would correspond to which "horizontal." This allows for study of an arbitrarily shaped particle, rather than requiring a standard reference shape such as a sphere or ellipsoid. For use in this paper, the original scans were simplified to achieve consistent baselines. All samples were simplified using cubes of size 50 and 500 μm. This allows even comparison between samples, with less concern about sampling differences due to the scanning and model construction process.

We also implemented the rms height roughness metric ξ detailed by Shepard et al. (2001) using the same method as our approach to rms slope. Equation (2) defines this metric, where z_i measures the distance from the centroid of the high-resolution model's face i to the local horizontal mean $\bar{z}$ defined by the low-resolution model, projected along the normal of the coarser face:

$$\xi = \sqrt{\frac{1}{N-1}\sum_{i=1}^{N}(z_i - \bar{z})^2}. \tag{2}$$

3.2.2. Angularity

Sample angularity was analyzed using the gradient-based angularity index AI_g, as applied to 3D objects by Su et al. (2020). This method builds on previous work that used similar gradient angularity indices to characterize samples via 2D profiles, rather than 3D surfaces (National Academies of Sciences, Engineering, and Medicine 2007; Chen et al. 2016; Su & Yan 2018). Each sample had a limited-degree spherical harmonic series fit to its 50 μm model facets using the Python library `pyshtools` (Wieczorek & Meschede 2018). The spherical harmonic model was then evaluated at the angular coordinates of a near-spherical geodesic grid created through the Python library `meshzoo` (see Figure 3). Spherical harmonic models have previously been used in studying small particles' shapes, particularly aggregates for use in concretes (e.g., Garboczi 2002), without the need to record individual locations for each point on the particle surface. They have also been used extensively in a range of planetary applications, particularly in modeling small body shapes (e.g., Barnouin et al. 2019; Zuber et al. 2000), planetary topography (Wieczorek 2015), and gravitational (e.g., Zuber et al. 2013) and magnetic fields (e.g., Purucker 2008; Purucker & Nicholas 2010). The use of the spherical harmonic series allows for an arbitrary grid to be chosen for evaluating the surface's shape, and the geodesic grid helps correct any sampling irregularities that may be present in the original scans owing to complex, difficult-to-scan surfaces or other inherent difficulties with the 3D scanner. An additional benefit to the geodesic mesh is a reduction in computation time due to the known grid and predetermined list of neighboring facets that will be used in the calculation of AI_g and shared between all the samples.

For each facet i of the constructed spherical harmonic mesh, the angle between it and the neighboring facets $j \in [1, 2, 3]$ was calculated as $\theta_{ij} = \arccos(\hat{n}_i \cdot \hat{n}_j)$, where $\hat{n}$ is the normal vector projected out of the corresponding facet. The gradient-based angularity index for an individual facet is then simply the sum of the three angles:

$$\mathrm{AI}_{g,i} = \sum_{j=1}^{3}\theta_{ij}. \tag{3}$$

To get a single, global value AI_g across the entire mesh, the $\mathrm{AI}_{g,i}$ values were combined using

$$\mathrm{AI}_g = \frac{\sum_{i=1}^{N}\mathrm{AI}_{g,i}}{\sum_{i=1}^{N}\mathrm{AI}'_{g,i}} - 1 = \frac{\sum_{i=1}^{N}\sum_{j=1}^{3}\theta_{ij}}{\sum_{i=1}^{N}\sum_{j=1}^{3}\theta'_{ij}} - 1, \tag{4}$$

where AI'_g and θ'_{ij} are the corresponding quantities for a degree 1 (ellipsoidal) model of the same resolution. Thus, spheres and ellipsoids have zero angularity, and more round or cuboid samples have lower AI_g than more flattened or jagged samples.

3.3. Degree and Resolution of Spherical Harmonic Models

To evaluate AI_g using the method of Su et al. (2020), it was necessary to fit a spherical harmonic series to the shape of the scanned mesh and then reevaluate it on a geodesic grid. We tested the values of AI_g at various degrees and resolutions to

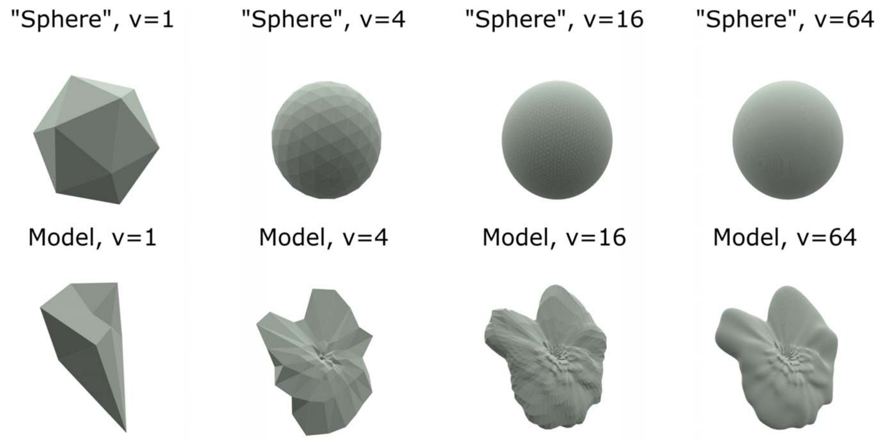

Figure 3. Evaluation of a geodesic grid on a sphere and the degree-25 spherical harmonic model of sample A-S-AllB-1 with geodesic frequency $v = 1, 4, 16, 64$. Higher-resolution models re-create the shape of the sample better but are limited by the accuracy of the finite-degree spherical harmonic model.

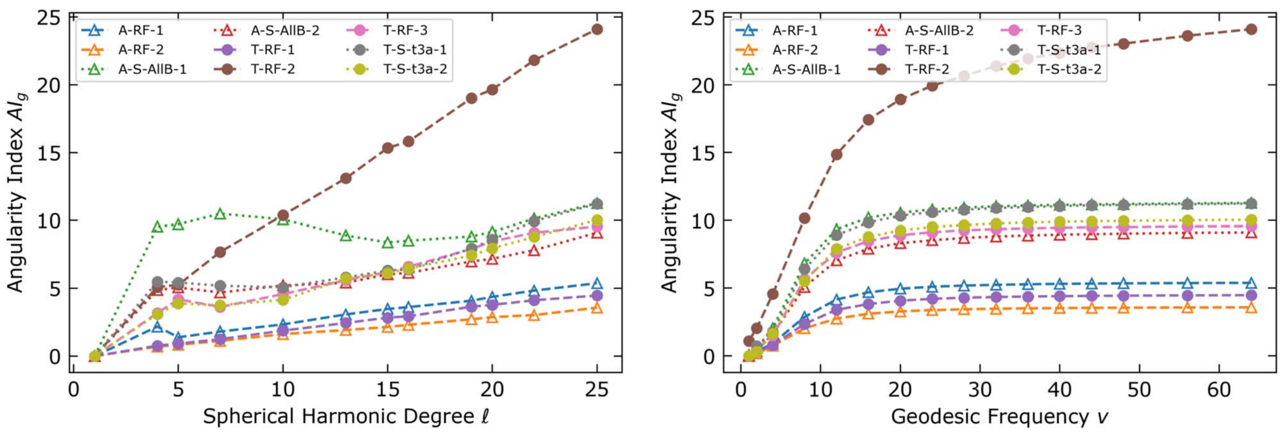

(a) Degree ℓ of the spherical harmonic fit (b) Geodesic frequency v of the output mesh

Figure 4. Plots showing the dependence of AI_g on spherical harmonic degree ℓ and output resolution as measured by the geodesic frequency v. The degree dependence is tested with $v = 64$; the frequency dependence is tested with $\ell = 25$. Samples from Allende are shown with upward-pointing triangles, while samples from Tamdakht are shown with filled circles. Additionally, "shard" samples (with flat surfaces present) have dotted lines, while "random fragment" samples have dashed lines. (a) As the spherical harmonic degree increases, the values of AI_g generally increase, but they do not all show the monotonically increasing behavior of the resolution dependence. They also do not show asymptotic behavior, making it difficult to define a cutoff. We use degree 25 for the calculations in this paper, following the method of Su et al. (2020). (b) As the number of faces increases, the values of AI_g appear to smoothly approach asymptotes. We use $v = 64$ for the calculations in this paper.

determine the optimal parameters to use. In order to perfectly reproduce the sample shapes, it would be necessary to have an extremely high degree spherical harmonic model. To help increase computational efficiency, we determined a cutoff to use for a "good-enough" model. Degrees 1–5 have been called "shape" and degrees 5–25 have been called "angularity" in previous work (Wang et al. 2005; Su et al. 2019, 2020). Figure 4(a) shows the dependence of AI_g on the degree ℓ of the spherical harmonic model used for nine selected samples. At $\ell = 1$, the samples all had $\mathrm{AI}_g = 0$, which matched the expectation from the definition of AI_g in Equation (4). At higher degrees, the values tended to increase (with some exceptions at relatively low degrees); however, they did not appear to be approaching any limit as the model degree increases. With no obvious improvement to be made, we used $\ell = 25$ for our AI_g calculations as in Su et al. (2020).

A Class I geodesic "sphere" of geodesic frequency v has $10v^2 + 2$ vertices and $20v^2$ faces, approaching a sphere as $v \to \infty$. This frequency measures the number of times an icosahedron's faces are subdivided before being projected into a sphere, with $v = 1$ being a 20-face icosahedron. Naturally, a higher-resolution model with more faces would more accurately depict the shape of the samples' spherical harmonic reconstructions. Figure 4(b) shows how the value of AI_g for a degree-25 model depended on geodesic frequency v for the same nine samples. The angularity index appeared to smoothly approach asymptotic values with increasing face counts. We found that $v = 64$, with 40,962 vertices and 81,920 faces, was sufficient resolution for an accurate measure. This agreed with the "icosa5" resolution chosen by Su et al. (2020) for their analysis of various angularity indices.

4. Results

Before calculating whole-sample values for θ_{rms} and AI_g, sample A-S-AllB-2 and all Aba Panu and Tamdakht shard samples had flat sections removed from their full 3D models. These sections are remnants of the original machined cubes and do not reflect the fracture roughness and angularity being analyzed here. The removed sections were left empty rather

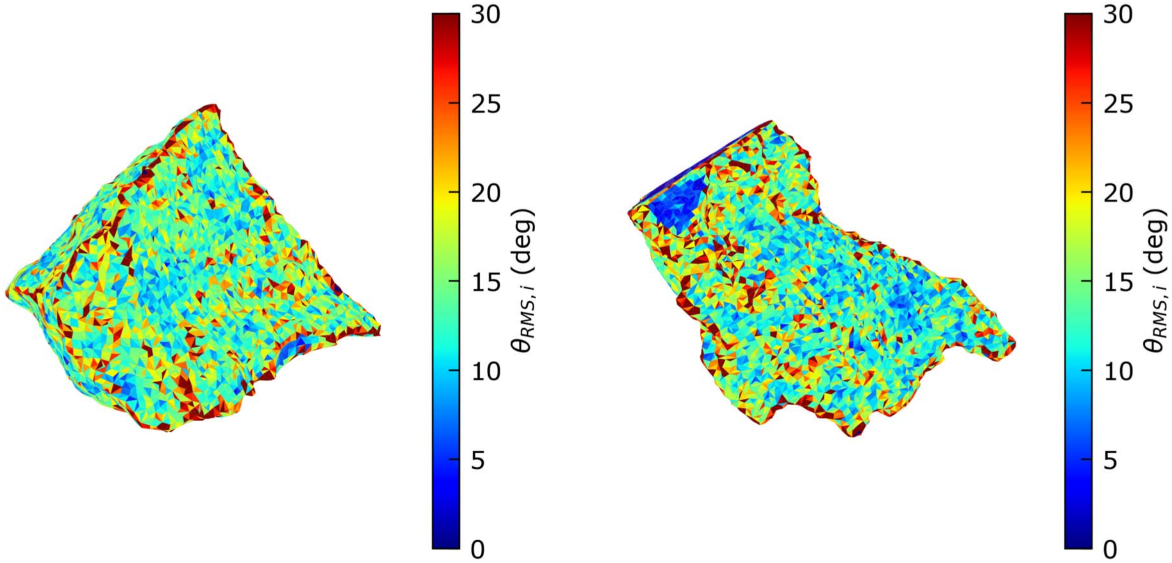

(a) Sample A-RF-1 (b) Sample T-S-t3a-2

Figure 5. 3D plot of local rms slope $\theta_{\mathrm{rms},i}$ distributed over the simplified model's faces. Each of these plots compares a 50 μm scale model to a 500 μm scale model. Local rms slope values on the color bar are measured in degrees.

than attempting to construct some representative section to fill in the gap.

4.1. Roughness

The rms slope θ_{rms} is calculated for a 50 μm model relative to a 500 μm model in order to obtain an even comparison between all the samples. We calculate both global roughness values, listed in Table 2, and local roughness values. Local roughness $\theta_{\mathrm{rms},i}$ is calculated via Equation (1), with the sum restricted to each of the 500 μm facets. Local roughness is plotted in Figure 5 for two selected samples. Global roughness values range from $14^{\circ}\!.59$ to $18^{\circ}\!.03$ for the Allende samples, from $16^{\circ}\!.87$ to $21^{\circ}\!.18$ for the Tamdakht samples, and from $17^{\circ}\!.10$ to $21^{\circ}\!.88$ for the Aba Panu samples. There is no clear separation in θ_{rms} values between samples from different meteorites, although the Allende samples are generally smoother than the Aba Panu samples by this metric. This still holds true even if the Allende RB samples, which may have been smoothed via contact with each other, are excluded.

In each of the plots in Figure 5, the brightly colored, high-value areas broadly align with fracture scarps near edges, while the lowest-value regions generally fall on smooth areas. In particular, the leftover machined faces that were removed for the global roughness analysis in certain samples are quite low in roughness value. Broader faces and the arcuate indentation in the lower right corner of Figure 5(a) also appear generally smooth. Notably, the Allende RB fragments (light-blue triangles in Figure 7) are consistently low in both roughness and angularity compared to other samples, which aligns well with the expectation for samples that were likely eroded while contacting each other in their bag. Future work should explore in more detail the effects of abrasion, especially as they would apply to larger bodies, but this serves as a preliminary check on the validity of our metrics.

Global and local rms height values showed little correlation with the rms slope metric or with other metrics examined here. Local height roughness ξ_i (evaluated in the same way as $\theta_{\mathrm{rms},i}$) revealed striped patterns on cut faces that were likely remnants of the cutting process.

4.2. Angularity

Once we have spherical harmonic models for our samples, we can calculate $\mathrm{AI}_{g,i}$ for the individual faces and AI_g values for the entire samples. As in Figure 5, we plot the spatial distributions of $\mathrm{AI}_{g,i}$ over the spherical harmonic models of the same selected samples in Figure 6. The $\mathrm{AI}_{g,i}$ values range over $\sim$3.5 orders of magnitude and as such are plotted in color and value on a $\log_{10}$ scale for clarity. This scale is also restricted to the range from $10^{-0.25}$ to $10^{1.8}$ deg for ease of comparison; this enhances the visual effect of "rounded" and "angular" areas. The global AI_g values vary more widely between the samples than the θ_{rms} values do and are listed in Table 2. Some sample edges have generally higher values of $\mathrm{AI}_{g,i}$ than their immediate surroundings, but similar values appear even on relatively flat or smooth portions of the samples. Additionally, very flat or jagged samples' $\mathrm{AI}_{g,i}$ distributions (particularly those of A-S-AllB-1 and T-S-t3a-2) appear to reflect the spherical harmonic models' structure more than the actual samples.

4.3. Metric Correlation

With the AI_g and θ_{rms} values calculated, we examine their correlation in Figure 7. Each sample source (either a shattered cube or random bag or fragment) is plotted using a different marker, with Allende samples plotted with triangles, Aba Panu samples with squares, and Tamdakht samples with filled circles. For collections with three or more samples, we perform linear regression analysis and plot the best-fit linear function as a dashed, dashed–dotted, or dotted line of the same color as the relevant points. The legend also lists the Pearson correlation coefficient r for each linear regression. These r values may suggest a correlation either stronger or weaker than is truly present owing to the limited sample sizes involved. The linear regression results vary significantly in best-fit slope, including both positive and negative correlations. Correlation strength

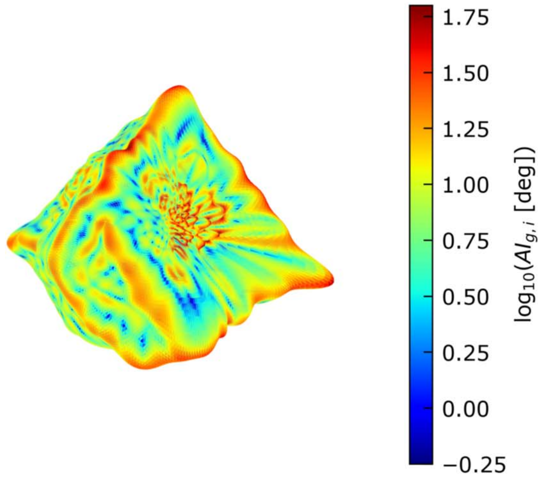

(a) Sample A-RF-1

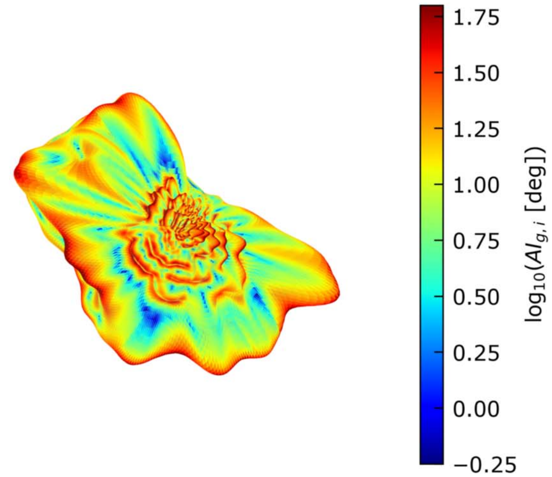

(b) Sample T-S-t3a-2

Figure 6. 3D plots of $\mathrm{AI}_{g,i}$ over the surfaces of the scanned samples. Color (and the values of $\mathrm{AI}_{g,i}$ in the color bars) for these figures is on a $\log_{10}$ scale, restricted to the range from $10^{-0.25}$ to $10^{1.8}$ deg.

also varies widely, to the extent that defining a linear relationship for some collections appears unreasonable. Notably, the Allende RB samples, shown as blue triangles, are in the lower left corner of Figure 7, in agreement with our expectation of results for somewhat abraded samples.

4.4. Strength and Homogeneity Dependence

Finally, we attempt to correlate rms slope values with strength properties for Allende and Tamdakht, using compressive strength σ and Weibull parameter m values from Cotto-Figueroa et al. (2016). We expect that samples from a more homogeneous meteorite should generally show smoother fracture surfaces. It should be noted that both properties describe the cube or meteorite from which the shards originated, not the compressive strength of any particular sample presented here or the homogeneity of those strengths. Figure 8 plots the θ_{rms} values for all the shard samples versus compressive strength (Figure 8(a)) and for all the Allende and Tamdakht samples (including “RF” and “RB” samples) versus Weibull parameter (Figure 8(b)). Aba Panu samples are excluded from Figure 8(b), as the Weibull parameter is currently unknown; however, Aba Panu is believed to be more homogeneous than either of the other two meteorites (Gabriel et al. 2021) and therefore should have higher Weibull m.

Figure 8(a) shows little overall correlation between strength and roughness, although there is a downward trend in roughness with increasing σ at high compressive strength values. Significant variation in θ_{rms} at lower strength values creates difficulty in defining a simple relationship between rms slope and strength. On the other hand, we do observe the expected trend with Weibull parameter m, as Tamdakht samples have on average higher rms slope values than those of Allende, as well as greater spread, correlating with Tamdakht’s lower m. Due to the limited data set, we include all the samples in these plots where possible; however, we note that the Allende RB fragments, having been stored loosely, may have been abraded and therefore may show reduced surface roughness. Further study of additional experimentally broken Allende shards is needed to strengthen this analysis. As we have neither a known m nor a range of strength values, our ability to comment on Aba Panu’s properties is limited. This meteorite is significantly stronger than either of the other two (Rabbi et al. 2021); however, its ranges of roughness and angularity are similar to those of Allende and Tamdakht. The sample with the highest calculated rms slope θ_{rms} was a shard from Aba Panu, but further study is needed for any strong claims.

5. Discussion

5.1. Roughness

Our approach using models limited to 50 and 500 μm facet sizes allows for a fair comparison between samples of different sizes. Additionally, each low-resolution facet includes approximately 100 high-resolution facets, reducing noise that might result from low relative facet counts. Future work may explore smaller facets (e.g., 10 μm compared to 50 μm models). Our choice of resolution was based on the scanning instrument’s accuracy and precision, as well as the original unsimplified models’ point spacing. We chose 50 μm spacing as being only slightly coarser than our lowest-resolution models, and we chose the 500 μm model in order to have sufficient facet counts relative to the high-resolution model and reduce the variability in our roughness metrics at low face counts (Susorney et al. 2019). Future work should explore different resolutions to examine how they may affect results, including alternative scanning methods that may allow for coarser or finer measurement.

Our global θ_{rms} roughness values are somewhat lower than those reported by Avdellidou et al. (2020), who measured roughness profiles in 5 cm diameter craters they created in larger blocks of carbonaceous asteroid simulant, 32°. However, this is at a larger scale and a different material. Our measurements are also lower than the roughness estimations based on thermal modeling of a boulder surface on asteroid (162173) Ryugu (Grott et al. 2019, 28°.7). Here the difference might again be attributed to different material properties and scales, but we also point out that it is a thermal model coefficient, not a roughness measurement per se. This illustrates our broader goal of comparing meteorite-based results to asteroid remote sensing measurements and suggests

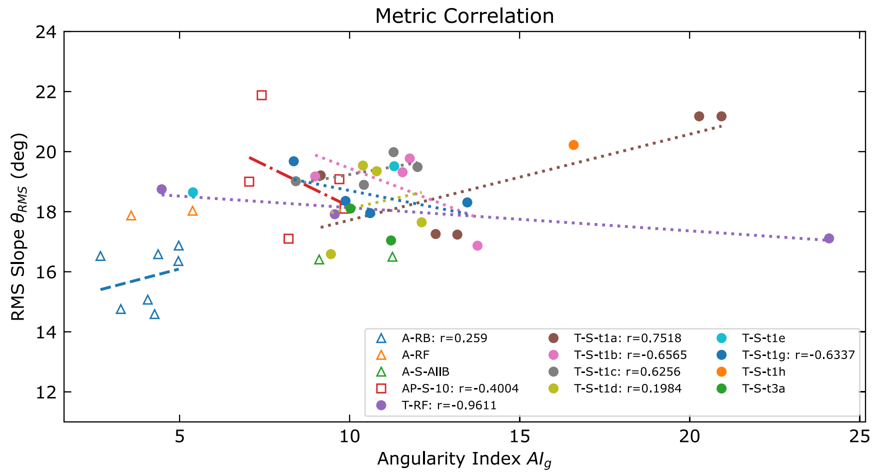

Figure 7. Plot of whole-sample values of AI_g vs. θ_{rms}. Allende samples are plotted with triangles and dashed lines, Aba Panu samples with squares and a dashed–dotted line, and Tamdakht samples with filled circles and dotted lines for each sample source. Best-fit lines are plotted for each collection with three or more members, and correlation coefficients r are provided for each; however, correlations appear subtle and inconsistent at best.

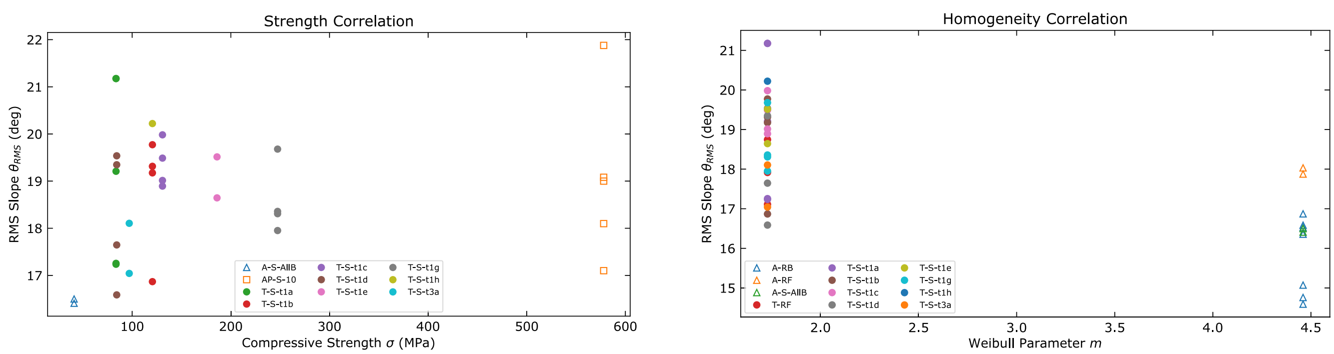

(a) (b)

Figure 8. Plots illustrating the dependence of θ_{rms} on strength properties. The rms slope and strength show little correlation. However, average roughness is lower for the higher-m Allende samples. (a) Plot of rms slope vs. compressive strength σ for all shard samples. (b) Plot of rms slope vs. Weibull parameter m for Allende and Tamdakht samples.

how optical measurements of roughness might be combined with other spacecraft data.

Local roughness appears to be accurately described by $\theta_{\mathrm{rms},i}$, as the highest-value areas in Figure 5 generally align with edges on the samples, while low-value areas align with generally smoother regions. Samples from all three meteorites tested here overlap in global θ_{rms} values, preventing any sort of separation based on global roughness alone. Even using higher-resolution scanning methods including optical and electron microscopes, Nagaashi & Nakamura (2023) failed to find significant separation in cohesive strength of meteorite powders between different samples, despite visibly different particle surface morphologies under the electron microscope. Future work could include analysis of the scale dependence of the roughness metrics presented here, along with other metrics, using higher-resolution 3D scanning methods to allow for a broader range of feature sizes to be included.

Figure 9 shows the histogram (solid lines) of $\theta_{\mathrm{rms},i}$ values for each sample using 250 bins. The histograms all show similar distributions of values that can be well modeled by a lognormal distribution, drawn with a dashed line for each sample's data. These experiments could potentially be compared with returned asteroid samples at smaller scales. Future work should examine different measurement baselines to test the scale and resolution dependence of this calculated roughness. Additionally, roughness properties of different lithologies of the samples should be examined. Relative proportions of calcium–aluminum-rich inclusions, chondrules, and matrix-like components were not considered here but may influence the spread in data we observe or show additional, useful textural properties. The effects of abrasion should also be explored in more detail, to determine more thoroughly how particles' textural and strength properties may evolve through contact with each other and through other processes.

5.2. Angularity

The range of values of AI_g is much wider than the range of θ_{rms} values. This reflects the wide range of different shapes that the samples have. In particular, the more rounded or cuboid samples (A-RF-1, A-RF-2, T-RF-1) have relatively low values, while the more flattened and/or jagged samples have higher angularity values. This agrees with the prior expectation for which samples might be more "angular." As with the θ_{rms} values, there is no clear separation between samples from different meteorites. The AI_g values for samples with broadly similar shapes (e.g., A-RF-1, A-RF-2, and T-RF-2) are similar,

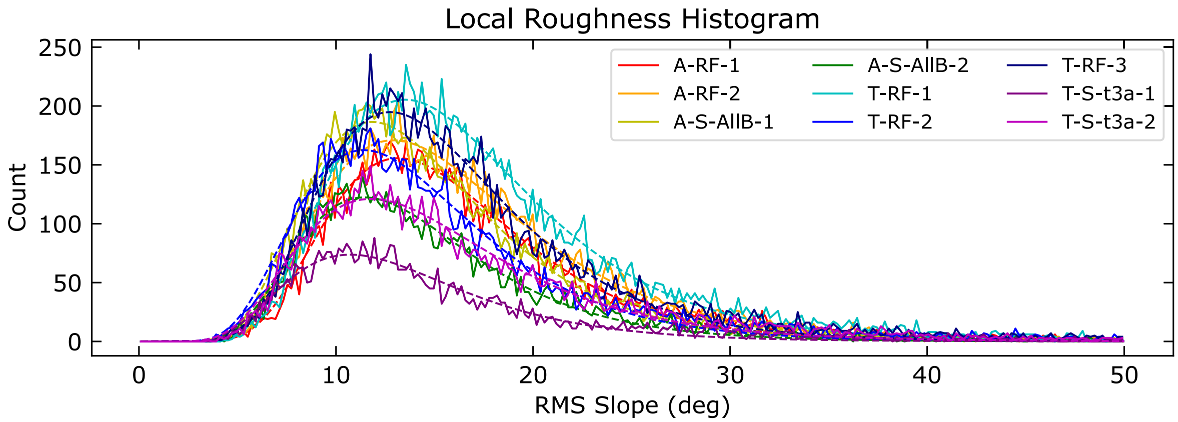

Figure 9. Histogram of $\theta_{\mathrm{rms},i}$ values for the nine samples shown in Figure 1. Histograms are drawn with solid lines. The best-fit lognormal distribution is drawn with a dashed line for each sample. These histograms use 250 bins linearly spaced from 0°.1 to 50°. The distribution is similar for coarser or finer binning.

not only for the chosen model parameters but also at almost all model degrees and resolutions tested in Figure 4.

The shapes of the 3D plots in Figure 6 illustrate the 25th-degree spherical harmonic models of the samples. Even at the chosen target, degree 25, the spherical harmonic models fail to capture the sharp edges of the samples. This is true for all nine samples but is especially clear for the highly jagged sample T-S-t3a-2, shown in Figure 6(b). Higher-degree models capture slightly more of the angularity, but it would take an extremely high degree model to fully capture the samples' angularity and separate similarly shaped samples. The models describe the more cuboid samples (e.g., A-RF-1, Figure 2(a)) somewhat more accurately but still fail to precisely capture sample edges. The data suggest that the angularity metric AI_g, as defined and applied by Su et al. (2020), is insufficient to describe these highly angular samples and is better suited to relatively round or equidimensional particles. This method was developed by Su et al. (2020) using subrounded cobblestones and subangular to angular ballasts, which lack the complex edges and/or highly flattened shapes of some of our samples. These effects will lead to unrealistic spikes in the spherical harmonic model, visible on both plots in Figure 6 and others. These spikes then increase the calculated angularity index AI_g.

There are also risks to this approach. The original 3D model of the sample is used for fitting the spherical harmonic model, and the output fit is somewhat dependent on the input model's resolution. Additionally, any errors present in the creation of either model will be compounded in this fitting step. Sample T-RF-2 in particular had a significant feature that appeared in the spherical harmonic model fit to the 50 μm model but was absent when fitting to the original unsimplified model. This additional feature creates a dramatic increase in the calculated angularity index, from 11.06 to 24.21. It is possible that using an optical or electron microscope or other method to achieve a higher-resolution model than is possible with our optical scanner could affect results. This would likely have a more significant impact on the roughness metrics than the angularity metric; however, adjustments to the angularity model to allow for higher-degree variations could be considered. The $\mathrm{AI}_{g,i}$ distributions appear to be dominated by the ringing effects of the finite-degree model rather than the actual shape of the meteorite samples. Still, the general trend of AI_g values seems to describe "rounder" versus more angular samples reasonably well.

5.3. Metric Correlation and Connection to Strength

A correlation, if any, between roughness and angularity in the Allende, Tamdakht, and Aba Panu samples is obscure. Figure 7 shows significant variation in correlation slope and correlation strength even within the Tamdakht samples, with roughness and angularity being positively or negatively correlated to varying degrees. A larger sample size can always help strengthen conclusions, but given the results here, there is little indication that these metrics are well correlated for meteorite fracture surfaces, especially in such a way as to be distinguishable between different meteorites.

For strength properties, we focus on testing the correlation of measured compressive strength values with rms slope, as we have found it to describe samples more accurately than angularity. Our ideal outcome would be identifying correlation such that optically measurable roughness could act as a constraint on material strength. Even a relatively weak constraint could be of high utility, potentially linking remote sensing properties of meteorites and even asteroids to strength properties that are critical for planetary defense planning. Despite our efforts, we find little correlation between fracture surface roughness and compressive strength, shown in Figure 8(a). The data do not appear to follow a simple relationship such as a linear function, and the spread of roughness values even for samples from the same cube makes it difficult to define any more complex function with confidence. The angularity index AI_g shows a similar lack of correlation.

Finally, we consider the correlation of roughness properties with the source meteorites' Weibull parameters m. Given the limited sample with only two different meteorites of known m and the limited study of our third meteorite, Aba Panu, it is not possible to draw strong conclusions. Still, Figure 8(b) aligns with our expectation that the more homogeneous (lower m) Allende samples should on average have lower roughness, even if the potentially smoothed RB samples are excluded. Aba Panu, however, is expected to be even more homogeneous than Allende (Gabriel et al. 2021) yet has higher average roughness.

5.4. Future Work

Future work should expand this sample set with additional samples from Allende and Aba Panu, as well as additional meteorites or other rocks of known m, to further test the connection between strength homogeneity and roughness.

The Hurst exponent for the samples may be studied, i.e., how the two roughness metrics change for different baselines, created via finer or coarser sample models. Surface roughness spectra were previously explored by Persson & Biele (2022); however, they used a limited sample of three chondrite particles, and further investigation is merited particularly in attempting to apply our analyses to larger, asteroid-scale bodies and features. Part of the study of scale dependence of these textural properties should include a broader range of sample sizes than examined here, to better model whether useful surface fracture measurements are possible using remote sensing. Su et al. (2020) found that their gradient-based and curvature-based angularity indices (AI_g and AI_G) were well correlated for their samples, with different power laws for different classes. We are exploring the possibility of a similarly distinguishable relationship for different meteorites or meteorite classes.

More fundamentally, we may be looking for simple trends when the correlations are more complicated than, e.g., roughness and angularity indicating strength. A more careful examination of the ensemble fragments (per meteorite) is required to understand how measured quantities correlate not to strength but to strength heterogeneity in a meteorite type, for example. In addition to the reported strength values, there is also the post-peak stress behavior after failure that is recorded in experiments but has yet to be included in any structural analysis of meteorites. Other fracture-related properties, such as fracture toughness (Lange et al. 1993) and porosity, which also correlates with strength (Lian et al. 2011), can be added to the data for analysis. It could be that the correlations are between sets of variables in a larger parameter space than is considered in this initial study.

6. Conclusions

To be able to predict the strength properties of asteroid materials based on remote sensing quantities would be of great potential benefit for meteorite research, solar system science, and planetary defense. This is a first evaluation of that possibility, a search for correlations between strength properties and the visible morphology of fractured surfaces in meteorites.

This study did not identify any clear relationships between the parameters that were studied, and we find that important questions remain regarding resolution and the consideration of different fracture sources due to impacts (Cambioni et al. 2021), thermal fatigue (Delbo et al. 2022), and abrasion. The relatively small statistical sampling so far, especially for Allende and Aba Panu, indicates the need to apply these methods to a larger collection of strength-tested samples of those meteorites and to expand the study to other meteorites and other measurable parameters. This may reveal dependencies that are not apparent in the current data set.

A significant complicating factor with meteorite to asteroid scaling is the well-known bias of meteorites, as these have survived ejection from their parent body, transport through space, and passage through Earth's atmosphere and impact on the surface. The material that survives as meteorites is likely composed of some of the strongest portions of the source. Furthermore, the fragments of disruption experiments are always stronger than the original specimen. The results of the Hayabusa2 (Watanabe et al. 2017) and OSIRIS-REx (Lauretta et al. 2017) asteroid sample return missions will aid in understanding those relationships. While these biases present a major challenge, they are also a primary motivation for this research, as a systematic bias may be related to the variation of strength properties and roughness properties within specimens obtained from the same intact meteorite (Cotto-Figueroa et al. 2016). The study of such variations might lead to an extrapolated knowledge of the behavior of the larger, presumably weaker rocks and boulders on asteroids (Ballouz et al. 2020). Future application of our methods to returned samples from asteroids would help clarify the relationship between meteorites and asteroid-scale bodies. While our investigation shows that making these correlations is not as simple as mapping surface roughness to strength, the correlation with strength heterogeneity is interesting. More laboratory analysis is required on these and other samples as they become available in strength-to-failure experiments, as well as meteorite falls with fresh fracture surfaces. It remains to be seen whether roughness and angularity or similar metrics are sufficient to reveal the strength properties at an asteroid's larger scale, or whether additional remote sensing measurements can resolve that question.

Acknowledgments

This material is based on work supported by the National Aeronautics and Space Administration (NASA) under grant No. 80NSSC21K1983 issued through the Yearly Opportunities for Research in Planetary Defense (YORPD) Program. We gratefully acknowledge the use of lab space and equipment funded through the OSIRIS-REx mission (NASA Contract NNM10AA11C) for the scanning of our samples, and the Buseck Center for Meteorite Studies for providing the meteorites.

ORCID iDs

Gabriel Gowman https://orcid.org/0000-0002-0644-2956
Desireé Cotto-Figueroa https://orcid.org/0000-0002-5468-1564
Andrew Ryan https://orcid.org/0000-0002-7535-8416
Laurence A. J. Garvie https://orcid.org/0000-0003-2038-3435
Christian G. Hoover https://orcid.org/0000-0002-0073-2768
Erik Asphaug https://orcid.org/0000-0003-1002-2038

References

Avdellidou, C., Di Donna, A., Schultz, C., et al. 2020, Icar, 341, 113648
Ballouz, R.-L., Walsh, K. J., Barnouin, O. S., et al. 2020, Natur, 587, 205
Barnouin, O. S., Daly, M. G., Palmer, E. E., et al. 2019, NatGe, 12, 247
Bell, T., Li, B., & Zhang, S. 2016, Structured Light Techniques and Applications (New York: Wiley), 1
Britt, D. T., & Consolmagno, G. J. S. J. 2003, M&PS, 38, 1161
Cambioni, S., Delbo, M., Poggiali, G., et al. 2021, Natur, 598, 49
Chen, S., Yang, X., You, Z., & Wang, M. 2016, Constr. Build. Mater., 120, 442
Cignoni, P., Callieri, M., Corsini, M., et al. 2008, in Eurographics Italian Chapter Conf. 2008, ed. V. Scarano, R. De Chiara, & U. Erra (The Eurographics Association)
Cotto-Figueroa, D., Asphaug, E., Garvie, L., et al. 2016, Icar, 277, 73
Delbo, M., Walsh, K. J., Matonti, C., et al. 2022, NatGe, 15, 453
Ficker, T., Martišek, D., & Jennings, H. M. 2010, Cem. Concr. Res., 40, 947
Flynn, G. J., Strait, M., Willman, H., et al. 2023, LPSC, 54, 1250
Gabriel, T. S. J., Cotto-Figueroa, D., Asphaug, E., et al. 2021, in 7th IAA Planetary Defense Conf. (Vienna), 224
Garboczi, E. 2002, Cem. Concr. Res., 32, 1621

Gattacceca, J., McCubbin, F. M., Bouvier, A., & Grossman, J. 2020, M&PS, 55, 460
Grott, M., Knollenberg, J., Hamm, M., et al. 2019, NatAs, 3, 971
King, E. A., Schonfeld, E., Richardson, K. A., & Eldridge, J. S. 1969, Sci, 163, 928
Lange, D. A., Jennings, H. M., & Shah, S. P. 1993, JACS, 76, 589
Lauretta, D. S., Balram-Knutson, S. S., Beshore, E., et al. 2017, SSRv, 212, 925
Li, S. J., Wang, S. J., Miao, B. K., et al. 2019, JGRE, 124, 2945
Lian, C., Zhuge, Y., & Beecham, S. 2011, Constr. Build. Mater., 25, 4294
Nagaashi, Y., Aoki, T., & Nakamura, A. M. 2021, Icar, 360, 114357
Nagaashi, Y., & Nakamura, A. M. 2023, SciA, 9, eadd3530
National Academies of Sciences, Engineering, and Medicine 2007, Test Methods for Characterizing Aggregate Shape, Texture, and Angularity (Washington, DC.: The National Academies Press)
Persson, B. N. J., & Biele, J. 2022, Tribology Letters, 70, 34
Purucker, M. E. 2008, Icar, 197, 19
Purucker, M. E., & Nicholas, J. B. 2010, JGRE, 115, E12007
Rabbi, M. F., Garvie, L. A. J., Cotto-Figueroa, D., et al. 2021, M&PS, 56, 2131
Rozitis, B., Ryan, A. J., Emery, J. P., et al. 2020, SciA, 6, eabc3699
Shepard, M. K., Campbell, B. A., Bulmer, M. H., et al. 2001, JGR, 106, 32777
Su, D., Wang, X., & Wang, X. 2020, Powder Technol., 364, 1009
Su, D., Wang, X., Yang, H.-W., & Hong, C. 2019, Powder Technol., 356, 423
Su, D., & Yan, W. 2018, Constr. Build. Mater., 161, 547
Susorney, H. C., Johnson, C. L., Barnouin, O. S., et al. 2019, Icar, 325, 141
Tsuchiyama, A., Uesugi, M., Matsushima, T., et al. 2011, Sci, 333, 1125
Wang, L., Wang, X., Mohammad, L., & Abadie, C. 2005, J. Mater. Civ. Eng., 17, 498
Watanabe, S., Tsuda, Y., Yoshikawa, M., et al. 2017, SSRv, 208, 3
Weisberg, M. K., Smith, C., Benedix, G., et al. 2009, M&PS, 44, 429
Wieczorek, M. 2015, in Treatise on Geophysics, ed. G. Schubert (2nd ed.; Amsterdam: Elsevier), 153
Wieczorek, M. A., & Meschede, M. 2018, GGG, 19, 2574
Zuber, M. T., Smith, D. E., Cheng, A. F., et al. 2000, Sci, 289, 2097
Zuber, M. T., Smith, D. E., Watkins, M. M., et al. 2013, Sci, 339, 668